A new z = 0 metagalactic UV background limit[*]

Joshua J. Adams

Department of Astronomy, University of Texas at Austin, 1 University Station, C1400, Austin, TX 78712

`jjadams@astro.as.utexas.edu`

Juan M. Uson

Observatoire de Paris - LERMA, 61 Avenue de l'Observatoire, 75014 Paris, France

Gary J. Hill and Phillip J. MacQueen

McDonald Observatory, University of Texas at Austin, 1 University Station, C1402, Austin, TX 78712

ABSTRACT

We present new integral-field spectroscopy in the outskirts of two nearby, edge-on, late-type galaxies to search for the Hα emission that is expected from the exposure of their hydrogen gas to the metagalactic ultraviolet background (UVB). Despite the sensitivity of the VIRUS-P spectrograph on the McDonald 2.7m telescope to low surface brightness emission and the large field-of-view, we do not detect Hα to 5σ upper limits of 6.4×10^{-19} erg/s/cm^2/$\square''$ in UGC 7321 and of 25×10^{-19} erg/s/cm^2/$\square''$ in UGC 1281 in each of the hundreds of independent spatial elements (fibers). We fit gas distribution models from overlapping 21 cm data of HI to create predicted Hα surface brightness models. Our principal analysis assumes that the gas extends beyond the 21 cm data limits in a regular manner. We analyze three types of limits from the data with stacks formed from increasingly large spatial regions and compare to the model predictions: 1) single fibers, 2) convolution of the fiber grid by a circular kernel ($10''$ full width half maximum), and 3) the coadded spectra from a few hundred fibers over the brightest model regions. None of these methods produce a significant detection ($> 5\sigma$) with the most stringent constraints on the HI photoionization rate of $\Gamma(z = 0) < 1.7 \times 10^{-14}$ s^{-1} in UGC 7321 and $\Gamma(z = 0) < 14 \times 10^{-14}$ s^{-1} in UGC 1281. The UGC 7321 limit is below previous measurement limits and also below current theoretical models. A second, weaker estimate is made with the UGC 7321 data based on the regions of overlapping 21 cm data yielding $\Gamma(z = 0) < 2.3 \times 10^{-14}$ s^{-1}, but with an analysis that does not assume a gas density extrapolation. We discuss how a low Lyman limit escape

---

[*]This paper includes data taken at The McDonald Observatory of The University of Texas at Austin.

fraction in low redshift star forming galaxies might explain this lower than predicted UVB strength and the prospects of deeper data to make a direct detection.

Subject headings: galaxies: evolution — diffuse radiation — intergalactic medium

1. Introduction

The strength of the metagalactic ultraviolet background (UVB) has great impact on theoretical models of structure formation (e.g. Haardt & Madau 1996) and a variety of physical processes such as the inhibition of small halo collapse (e.g. Efstathiou 1992), the intergalactic temperature and ionization state of the intergalactic medium (IGM) (e.g. Hui & Gnedin 1997), and IGM metallicity determinations (e.g. Rauch et al. 1997a). The likely contributors to the UVB are active galactic nuclei and star formation in galaxies which appear (Schirber & Bullock 2003; Faucher-Giguère et al. 2008b) compatible with observed populations (Gallego et al. 1995; Hopkins 2004; Hopkins et al. 2007; Bouwens et al. 2009) under reasonable corrections such as for dust attenuation, low luminosity extrapolations, redshift evolution, and escape fractions. The strength of the UVB, especially at low redshift (Davé & Tripp 2001), is still highly uncertain despite its importance. Most recent efforts have focused on high redshifts, $z > 2$, where the strongest UVB measurements exist. For instance, the detailed history of star formation (Madau et al. 1999; Faucher-Giguère et al. 2008a) and the potential to measure individual active galactic nuclei (AGN) host halo masses (Loeb & Eisenstein 1995; Faucher-Giguère et al. 2008c) have been explored. Measurements of the photoionization rate have used three methods: observations of Hα such as described in this paper, the line-of-sight proximity effect method (e.g. Carswell et al. 1982; Bajtlik et al. 1988), and the flux decrement method (e.g. Cen et al. 1994; Rauch et al. 1997b). The latter two require backlighting quasars and are therefore difficult or impossible at low redshift. We are motivated to constrain the current model with a different, low redshift measurement. Instead of using Lyman-α forest features, we pursue a measurement of the UVB powered, Hα emission that should occur in the outskirts of local disk galaxies. As a secondary motivation, the kinematics of Hα at distances beyond HI data are important probes to the total dark halo masses in nearby disk galaxies (Christlein & Zaritsky 2008).

Galactic disks are optically thick to Lyman limit photons and maintain their observed HI distributions through self-shielding against the UVB. As recognized for decades (Sunyaev 1969; Felten & Bergeron 1969; Bochkarev & Sunyaev 1977), the influence of the UVB may be investigated in the extreme outskirts of disks where the self-shielding begins to fail. These early works sought to measure this effect through disk truncation in HI. However, there appear to be cases with (Corbelli et al. 1989; van Gorkom 1993) and without (Walsh et al. 1997; Carignan & Purton 1998; Oosterloo et al. 2007) HI truncations above the critical column density predicted using current UVB estimates, implying that other processes may strip gas and mimic the result. Moreover, reaching the UVB implied truncation thresholds in 21 cm measured HI would require rather long observations with

current facilities. A more robust signature of the UVB strength would be the detection of the Hα in these outskirt regions. Hα has been found at such radii before in actively star forming and warped galaxies by Bland-Hawthorn et al. (1997) (hereafter BFQ) with Fabry-Perot staring measurements. However, the $\mu(H\alpha) = 2.3 \times 10^{-19}$ erg/s/cm^2/$\square''$ detection was interpreted to be due to non-UVB sources as indicated by an abnormally high [NII]λ6548 to Hα ratio. Searches have also yielded limits in quiescent systems (Vogel et al. 1995; Weymann et al. 2001; Madsen et al. 2001) with an upper limit for the UVB photoionization rate, Γ, of $\Gamma(z = 0) < 2.4 - 9.5 \times 10^{-14} \text{s}^{-1} (2\sigma)$ being the deepest. The wide range due on this limit is due to gas cloud geometrical uncertainty. Despite the numerous theoretical implications and the efforts of numerous groups, a UVB powered Hα detection still awaits discovery.

The tactical advantages we bring to this problem are deep surface brightness limits, a large two dimensional field of view through integral field spectroscopy compared to the previous longslit and Fabry-Perot staring data, and target selection of very high inclinations to maximize signal and minimize contamination uncertainty. Our targets are edge-on, low surface brightness Sd galaxies that are rather isolated and minimally warped in order to avoid density distribution uncertainties and exposure to internally generated ionization from smaller radii. Indeeed, our most constraining target, UGC 7321, has a gas surface density below that required for significant star formation (Kennicutt 1989) at all radii, as well as being unusually isolated with no known companions and minimal ($< 3°$) warping (Uson & Matthews 2003). In addition, the HI observations of UGC 7321 are amongst the most sensitive such measurements published to-date. That data allows a very precise model to be made for the gas distribution in the galaxy outskirts at the locations where we search for Hα emission.

Those data is plural

In this paper we begin with a description of the simple ionization state and density model of disk galaxies that will be used to link a measured Hα surface brightness with a particular UVB photoiozation rate in §2.1. In §2.3, we give disk parameter constraints based on fits to existing 21 cm data. Next, in §3, we present deep integral field spectroscopy observations at radii corresponding to the outermost detections of 21 cm emission and beyond. We describe the choices made to stack spectra on various spatial scales. The stacked spectra are searched for Hα detections and upper limits are derived. Particular focus is given to systematic errors. Finally, in §4, we discuss the context, the likely cause of the unexpectedly low limit, and further observations that can confirm our conclusions. The Appendix A provides the analytic details necessary to construct the full and general Hα surface brightness distribution model. We will quote most of the surface brightness limits in units of erg s^{-1} cm^{-2} arcsec^{-2}, but for easy comparison to alternative units we note the conversion at the wavelength of Hα of 1 millirayleigh (mR)$= 5.66 \times 10^{-21}$ erg s^{-1} cm^{-2} arcsec$^{-2} = 2.8 \times 10^{-3}$ cm^{-6} pc in emission measure assuming the case B coefficient we adopt.

2. HI based models and Hα predictions

2.1. Model assumptions

A three dimensional gas density distribution must be inferred in order to translate Hα surface brightness into a UVB strength. BFQ make predictive calculations assuming exponential forms both radially and vertically in the gas distribution with a plane parallel assumption. Motivated by the regular HI structure on local scales (García-Ruiz et al. 2002; Uson & Matthews 2003) of our chosen targets showing simple exponential trends and needing an extrapolated model in gas density for interpretation of UVB limits, we also assume exponential forms.

In order to interpret Hα measurements generically inside and outside of the UVB photoionization front around gaseous disks, we have generalized the model of BFQ. Some toy calculations in the model also show the importance of high inclination selection to make the deepest possible UVB constraints. This high inclination boon has been known before, but not carefully followed in earlier works' target selection. The model assumes both regular gas distributions and sharp photoionization transitions in a plane parallel approximation under arbitrary disk inclinations and sight lines. Our model assumes sharp photoionization fronts exist. We verify this assumption by estimating the Lyman limit photon mean free path at the midplane ionization front. In their Equation 3, BFQ estimate the hydrogen density at this point as $n_H \approx 0.05 \text{cm}^{-3}$. The Lyman limit photon mean free path is given by $l_{mpf} \approx (n \times a_\nu)^{-1} \approx 1.1 \text{pc}$ with a_ν (Osterbrock & Ferland 2006) as the hydrogen Lyman limit photoionization cross section. This is much smaller than the common disk scale lengths in either direction. The vertical scales for cold disk galaxies are of order 100 pc or greater. More sophisticated models can be made (Maloney 1993; Dove & Shull 1994) by solving for the ionization and excitation states of hydrogen and helium with full radiative transfer solutions in a grid of plane-parallel gas layers, but such an analysis is beyond the scope of this work.

The forthcoming derivation follows BFQ equations 1-6. The important differences are that this derivation is generalized for any viewing inclination, i, and for arbitrary positioning of the spectral data in the galaxy's field of observation. The BFQ derivations were specifically for $i = 0°$ and the field position along the major axis where all gas is photoionized. We denote the generic surface brightness in Hα as μ. We denote μ_0 as the special case of the peak Hα surface brightness where the photoionization front intersects the disk midplane. Our results reduce to the BFQ values of μ_0 for $i = 0°$. In Equation 1 we give the assumed gas distribution in cylindrical coordinates R and z with radial scale-length h_r, vertical scale length h_z, and central hydrogen density n_0.

$$n_H(R, z) = n_0 \exp(\frac{-|z|}{h_z}) \exp(\frac{-R}{h_r}) \tag{1}$$

The commonly assumed form of the UVB spectrum is given in Equation 2 where ν is the frequency, ν_0 is the Lyman limit frequency, J_0 is the UVB strength at the Lyman limit in units of erg cm^{-2} s^{-1} Hz^{-1} sr^{-1}, and β is the UVB spectral index.

$$J_\nu = J_0 \left(\frac{\nu_0}{\nu}\right)^\beta \tag{2}$$

Another common form of quoting the UVB strength is with the UVB photoionization rate, Γ. We show this form in Equation 3 where h is Planck's constant, $\sigma(\nu)$ is the hydrogen photoionization cross section, and $a_\nu = \sigma(\nu_0)$ is the Lyman limit cross section. The final equality in Equation 3 comes from the standard power law approximation to the cross section shape (Osterbrock & Ferland 2006).

$$\Gamma = 4\pi \int_{\nu_0}^{\infty} \frac{J_\nu \sigma(\nu)}{h\nu} d\nu = \frac{4\pi a_\nu J_0}{h \times (3 + \beta)} \tag{3}$$

In Equation 4 we equate recombination and ionization rates under a plane parallel approximation. For the radial regions where any self-shielding can take place, we consider the top and bottom of the disk to each see incident flux from only half their total solid angle. We define n_e as the electron density, n_p as the proton density, ξ as the ionization fraction, α_B as the case B recombination coefficient, and $z_c(R)$ as the vertical distance down to which the photoionization front penetrates at radius R. We define ε as the volume filling factor, assumed to be spatially invariant. A clumpy gas distribution can, to first order, be represented by using this terms in the range between zero and one. With the assumption of sharp ionization boundaries, we can equate the gas densities as $n_e = n_p = \xi n_H$ at radii beyond the photoionization front.

$$\alpha_B \int_{z_c(R)}^{\infty} \xi^2 \varepsilon n_e(R, z) n_p(R, z) dz = \int_{\nu_0}^{\infty} \frac{2\pi J_\nu}{h\nu} d\nu = \frac{2\pi J_0}{h\beta} \tag{4}$$

We next define a threshold radius, r_c, to which the UVB penetrates fully through the disk plane, so $z_c(r_c) = 0$. The solution of Equation 4 leads to Equations 5 and 6.

$$r_c = (\ln(2\xi^2 \varepsilon \alpha_B a_\nu n_0^2 h_z \beta) - \ln(\Gamma \times (3 + \beta))) \times h_r/2 \tag{5}$$

$$z_c(R) = \begin{cases} \pm(r_c - R) \times h_z/h_r & : R \leq r_c \\ 0 : R > r_c \end{cases} \tag{6}$$

Next, we define the variable ρ as the distance from the disk's plane along the line-of-sight, spanning $-\infty$ to the observer and ∞ away from the observer. We also define the major axis position b_1, and minor axis position b_2 as the observed field positions projected onto the sky. Finally, we represent the galaxy's inclination with i. Simple transformations to cylindrical coordinates give the expressions in Equations 7 and 8.

$$|z| = \sqrt{\rho^2 \cos^2 i + b_2^2 \sin^2 i + 2\rho b_2 \sin i \cos i} \tag{7}$$

$$R = \sqrt{\rho^2 \sin^2 i + b_2^2 \cos^2 i + b_1^2 - 2\rho b_2 \sin i \cos i} \tag{8}$$

The Hα surface brightness, $\mu(b_1, b_2)$, then directly follows from a line-of-sight integration. The full evaluation of $\mu(b_1, b_2)$ involves finding the values of ρ that intersect the photoionization surface described by $z_c(R)$ with field positions b_1 and b_2. The analytic solutions to those intersections are given in Appendix A. The solution for the special case at field position $b_2 = 0$ and $b_1 = r_c$ gives the aforementioned peak surface brightness μ_0. μ_0 is itself a useful measurement parameter, as

related in Equation 9. In Equation 9, γ is the generally non-analytic integration of the emissivity along the line of sight, $\alpha_{H\alpha}^{\text{eff}}$ is the case B effective Hα recombination coefficient, and Ω is the full sky solid angle of 4π sr. For the gas density parameters we derive in our target galaxies in §2.3 and the areas we observe in §3, the face-on columns of total hydrogen are sufficient ($> 10^{17}$ cm^{-2}) to be everywhere optically thick to Lyman limit photons, let alone Lyman-β and the other important lower energy transitions. We use specifically use $\alpha_{H\alpha}^{\text{eff}} = 1.17 \times 10^{-13}$ cm^3 s^{-1} as appropriate for T$= 10^4$K (Osterbrock & Ferland 2006).

$$\mu_0 = \frac{2h\nu_{H\alpha}\alpha_{H\alpha}^{\text{eff}} \int_0^\infty n_e(R,z)n_p(R,z)d\rho}{\Omega} = \frac{2\xi^2\varepsilon\alpha_{H\alpha}^{\text{eff}}n_0^2 h\nu_{H\alpha}\gamma}{\Omega}$$
$$\text{with } \gamma = \int_0^\infty \exp\left(-\frac{2\rho\cos i}{h_z} - \frac{2\sqrt{r_c^2 + \rho^2\sin^2 i}}{h_r}\right)d\rho \tag{9}$$

We explain the use of certain constants and assumed values to Equation 9. The ionization fraction is assumed to be unity by the earlier discussion of the Lyman limit mean free path. The volume filling factor may approach unity as there is no indication of star formation at extended scales in these galaxies. We will discuss the evidence for the absence of extended star formation in Section 4. Furthermore, the deprojection of the HI distribution in Uson & Matthews (2003) gives a peak surface density of only 5.8 $M_\odot$ pc^{-2} at the center of UGC 7321. The surface density drops by over an order of magnitude at the locations we observe. These surface densities are well below the dynamical criterion for efficient star formation (Kennicutt 1989) and make a smooth gas distribution plausible. It is not possible to definitively show that the gas is without small scale clumpiness, so we retain the volume filling factor. The case B and Hα effective recombination coefficients are dependent on electron temperature. Following Weymann et al. (2001) and the discussion therein, we adopt T=10,000 K and the values of Osterbrock & Ferland (2006). The true electron temperature may plausibly be different by a factor of two, leading to corresponding changes in $\alpha_{H\alpha}^{\text{eff}}$ and α_B of the same order of magnitude. However, the linearization in Γ of Equation 9 makes the surface brightness depend on the ratio of these two recombination coefficients, so their similar behavior with electron temperature cancels. For consistency with previous works, we do not propagate the recombination coefficient uncertainties as systematics to the final UVB limit.

Some brief numerical examples set the expected orders of magnitude, quantify the achievable limits under different galaxy geometries, and illustrate the important parameter dependencies under linear expansions. We look at some trial cases with $\varepsilon = 1$, $h_r = 1000$ pc, $h_z = 100$ pc, $\beta = 1.8$, $\Gamma = 4 \times 10^{-14}$ s^{-1}, and $n_0 = 5$ cm^{-3}. For $i = 0°$, $\gamma = \exp(-2r_c/h_r) \times h_z/2$ so $\mu \approx 3.0 \times 10^{-20}$ erg/s/cm^2/□″. For $i = 90°$, $\gamma = r_c K_1(2r_c/h_r)$. $K_1(x)$ is the modified Bessel function. In this case, $\mu \approx 1.3 \times 10^{-18}$ erg/s/cm^2/□″. For this work's applications, the surface brightness profiles are smoothed by seeing and sampled by large fibers. Realistic smoothing and sampling, of order several arseconds size, can lower these peak values by several tens of percent. We will assume for all calculations that $\beta = 1.8$ as motivated by previous models (Shull et al. 1999) and to aid comparison with previous observational work using the same assumption (Weymann et al. 2001). We note that μ_0 scales exactly linearly with Γ when viewed face-on and nearly linearly for all other

inclinations. This is easily demonstrated by taking the large argument asymptotic behavior of the modified Bessel function which yields a linear scaling in Γ after a first order expansion. We check the error from linearization in Figure 1 for reasonable geometries. All further estimations of Γ in this work will be made in the linear approximation. The discussed numerical example between $i = 0°$ and $i = 90°$ also shows how the selection of thin, edge-on disks can exploit a particular flux limit to a $(30 - 50\times)$ stronger UVB constraint than for face-on disks. We also emphasize with Equation 9 that the first order effects near $i=90°$ on distance, volume filling factor, and gas density cancel out. μ_0 only has first order dependence on i, the ratio of scale lengths, $\frac{3+\beta}{\beta}$, and Γ.

2.2. Aspect ratio limit

The model for data comparison we have proposed in §2.1 is not the standard in UVB Hα searches. Instead, a single, simple equation based on global photoionization equilibrium is repeated here in Equation 10 from Weymann et al. (2001). Similar forms have been used in Stocke et al. (1991); Vogel et al. (1995); Donahue et al. (1995).

$$\Phi = \Gamma\frac{3+\beta}{4a_\nu\beta} = \frac{I_{H\alpha}}{f_a f_{H\alpha}}\frac{A_{proj}}{A_{tot}} \tag{10}$$

The variable Φ is the one-sided incident ionizing UVB flux in units of cm^{-2} s^{-1}, $I_{H\alpha}$ is the Hα surface brightness in units of μR, f_a is the fraction of incident photons that become absorbed when passing through the face-on cloud, $f_{H\alpha}$ is the fraction of excited recombinations that produce an Hα photon, A_{proj} is the projected area covered by spectroscopy and 21cm data, and A_{tot} is the total surface area for the regions in projection that can absorb Lyman limit photons. The area aspect ratio is usually determined from 21cm data. This calculation takes no account of the spatial stratification between 21cm and Hα that can realistically occur for highly thin gas distributions, as we will see later in Figure 2, and requires that Hα searches and interpretations are restricted to area covered by deep 21cm data. However, for mild aspect ratios ($\sim< 10$) or large 21cm beams, this method delivers similar predictions as those in §2.1.

We now discuss the evaluation of the few terms in this model. Our chosen pointings in UGC 1281 have very little overlap with existing 21cm data, see Figure 3, so we restrict the aspect ratio model discussion to UGC 7321. The assumption in the aspect ratio model is that the hydrogen resides within some well-defined area represented by the noise floor of the 21cm data. It is not obvious how the area should be defined in a continuous gas distribution, but we adopt the photoionization front we have previously defined in Equations 5 and 6 as a realistic edge. In §2.3 we determine gas geometries for our target galaxies. In particular for the area in UGC 7321 covered by fibers, with $N_{HI} > 10^{19}$ cm^{-2}, and the parameters in Table 1, we find $\langle\frac{A_{tot}}{A_{proj}}\rangle = 24.8^{+3.4}_{-1.5}$. This value is reasonable when compared to the 21cm axis ratio of 29 determined at the 10^{20} cm^{-2} contour in Uson & Matthews (2003, Table 3). By adopting this distribution in face-on column density and a UVB spectral index of $\beta = 1.8$, we can evaluate f_a. We find $\langle\frac{A_{tot}f_a}{A_{proj}}\rangle = 22.8^{+4.4}_{-1.8}$.
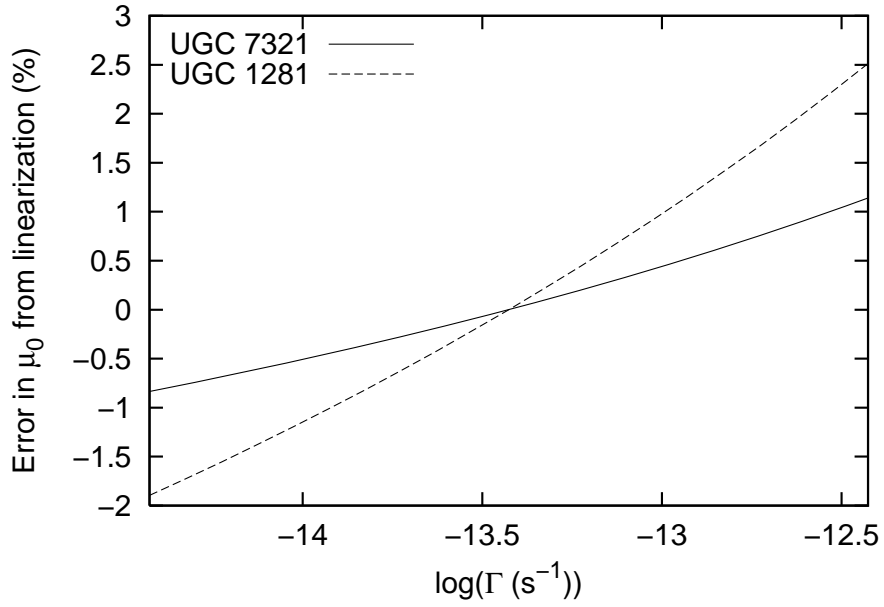
Fig. 1.— The error in linearization for the Hα peak surface brightness under different UVB strengths. The parameters for the two target galaxies are given in Table 1 and their derivation described in §2.3. The pivot in the linearization at $\Gamma = 4 \times 10^{-14}$ s^{-1} represents the current best estimate from Faucher-Giguère et al. (2009).

Identically to Weymann et al. (2001), we adopt $f_{H\alpha} = 0.45$ as appropriate for case B and a 10^4K electron temperature. We will carry out comparison to this model for UGC 7321 for continuity with previous work and to avoid an assumption of gas existing at observed distances and densities in these galaxies, but we emphasize that our preferred limit comes from the comparisons to the model in §2.1.

2.3. HI data

Structural values must be determined for individual galaxies to interpret Hα surface brightness and to guide the stacking choices amongst fibers. We will use such fits to extrapolate the density profiles to larger radii where the Hα emission is predicted to reach peak surface brightness. The parameters from stellar distributions could potentially be used, but 21 cm measured HI is the more relevant indicator to ionized hydrogen. We adopt distances of 10 Mpc for UGC 7321 (Uson & Matthews 2003) and 5 Mpc for UGC 1281 (Tully et al. 2006). Low redshift surface brightness is insensitive to distance, so the exact distances are unimportant to this work. Different literature estimations have 50% and 10% rms ranges for the UGC 7321 and UGC 1281 distances respectively. We indicate scale lengths by the terms d_{10} as the actual distance to UGC 7321 in units of 10 Mpc and d_5 as the actual distance to UGC 1281 in units of 5 Mpc. For reference, the scale conversions become $48.5d_{10}$ pc/$''$ for UGC 7321 and $24.2d_5$ pc/$''$ for UGC 1281.

UGC 7321 was observed by one of us in collaboration with L. D. Matthews (Uson & Matthews 2003) using the second most-compact (C) configuration of the VLA[1] which includes some of the shortest spacings available and their full coverage, deep observations yielded spacings down to 28m, close to the dish diameter. Their quasi-naturally weighted ("robust" parameter $\mathcal{R} = +1$) recovered the full single-dish flux and, moreover, their single-dish equivalent spectrum matched the features of the best single-dish spectrum to within the (higher) uncertainty of the single-dish observations (Uson & Matthews (2003), fig. 6). For this paper, we have used their quasi-uniformly ($\mathcal{R} = -1$) weighted images because of their better resolution ($\sim 12''$) although the somewhat higher (45%) noise level only recovers ~ 96% of the total flux. However, the 5 parameter model fits to the zeroth moment maps, described below, recover some of the lost flux and the remaining uncertainties should only shift slightly the position of the predicted Hα peak in Figure 3.

For UGC 1281, we have reduced the raw data from the VLA archive. It was observed under proposal AZ097 on 1997 December 26 in the most compact (D) configuration for a total of 3 hours on source with interspersed observations of the strong, primary calibrator J0137+3309 (3C48) for which we have adopted the VLA recommended flux density of 15.9 Jy. The observations were spaced over a range of ± 3 hours in H.A. giving excellent uv-coverage and images with 127 channels of width

---

[1]The Very Large Array of the National Radio Astronomy Observatory is a facility of the National Science Foundation, operated under cooperative agreement by Associated Universities, Inc.

~ 2.6 km s $^{-1}$ after standard on-line Hanning-smoothing. The angular scale that corresponds to the shortest baseline ($\sim 900''$) is sufficiently larger than the largest single-channel galaxy extent ($\sim 285''$) that the array should have recovered the total HI flux. We followed the same reduction steps as for UGC 7321 (Uson & Matthews 2003) to obtain a "cube" of spectral images using nearly-natural weighting ($\mathcal{R} = +1$) which gave images with resolution $\sim 51''$ which were free of artifacts to the rms sensitivity $\sigma \sim 1.0$ mJy/beam per channel. We computed moment maps after applying a standard "1-σ cutoff" evaluated on a cube Gaussian- smoothed spatially to $70''$ and Hanning-smoothed in frequency which led to a total HI flux of 41 ± 2 Jy km s^{-1} corresponding to a mass of $2.3 \times 10^8 \ d_5^2 M_\odot$. The total flux is in good agreement with the values in the literature which range from (35.8 to 38.9) Jy km/s from two different single-dish measurements (Huchtmeier 1989) with the spread and uncertainty due in part to some ringing from strong in-band HI emission from the Milky Way as well as to calibration uncertainties. Again, we have obtained a spectral "cube" with nearly-uniform weighting ($\mathcal{R} = -1$) which gave images with resolution of $\sim 42''$ with rms sensitivity $\sigma \sim 1.5$ mJy/beam per channel. As in UGC 7321, the higher noise level results in a slightly lower total flux, 39 ± 2 Jy km s^{-1}.

The HI data nearest the Hα observations is next characterized. We have derived five parameter fits in n_0, h_r, h_z, i, and position angle to the zeroth moment maps of UGC 7321 and UGC 1281 through non-linear least squares minimization. The models include convolution to the instrumental beams of $\sim 12''$ and $\sim 42''$ FWHM and sampling of Hα appropriate to the fiber data. Both the maps show at least two major axis power law slopes, as Christlein et al. (2010) have found to be common in extended gaseous disk gas. We do not try to model the full gas distributions, but only the large radius trends by restricting the fits heavily to the outermost data regions. Still, the model fits deviate from the data by an amount that exceeds the observational errors. Some minor warps and substructure are visible. The formal errors in the total line intensity images are 15×10^{18} cm^{-2} for UGC 7321 and 5×10^{18} cm^{-2} for UGC 1281, which are both far smaller than the residuals evident in Figure 2. In order to capture the systematic model errors, we have made Monte Carlo simulations between the data and the best fit models to create 68% confidence intervals as given in Table 1 for all disk parameters and Hα observables. The perturbations in the Monte Carlo simulations are made from the residuals of the best fit model, not the statistical errors, to include the influence of systematics. These simulations allow us to create three types of Hα surface brightness prediction, with different scales of spatial co-addition, under an assumed Γ. Note that many of the individual disk parameters in Table 1 have large relative uncertainties, but the surface brightness predictions have small relative uncertainties. The disk parameters share degeneracies, as captured in the Monte Carlo simulations, to create highly certain Hα predictions. Predictions can be made for individual fibers, but to both mitigate the model uncertainties and improve the data limits, we include predictions with a Hα $10'' \times 10''$ FWHM convolution sampled at the peak surface brightness positions. The exact choice of kernel size is not important, but chosen to include several neighboring fibers. Finally, we include a prediction for the average surface brightness of all fibers expected to sample $\mu > 10^{-19}$ erg/s/cm^2/$\square''$. These various predictions will be compared to co-added data in §3. We give in Figure 2 the HI fits along major and minor axis cuts. The fits to UGC 7321 use

all the HI data beyond an inner radius cut. That cut was chosen to avoid a substructure bump near $R \approx 140''$. The fits to UGC 1281 are more constrained with both an inner and outer radius cut. The outer cut is to exclude a known $\sim 8°$ warp (García-Ruiz et al. 2002). The fitting function assumes a single position angle at all radii and does not describe warps well. We have investigated the disk's outer behavior by also deriving fits from the R>220'' data alone. A radial scale length compatible with, but noisier than, the Table 1 value was found with a significant change in position angle as symptomatic of a warp.

3. Hα data and analysis

We have obtained new integral field spectroscopy positioned along the major axes of UGC 7321 and UGC 1281 targeting Hα with the Visible Integral-field Replicable Unit Spectrograph Prototype (VIRUS-P, Hill et al. 2008) on the McDonald 2.7m telescope. We observed UGC 1281 on 2009 October 22-24 with R = 1288 from 4700-6990Å for 21 photometric hours and UGC 7321 on 2010 April 9 and 11 with a resolution of R = 3860 from 6040-6740Å for 15 hours under non-photometric conditions. Between the R = 1288 and R = 3860 observations, made possible by a new grating, we not only gain in sensitivity scaled by the square root of the resolution but resolve the bright skylines, OH λ6568.779 and geocoronal Hα, from our target wavelengths. We have set the controller to bin pixels by two in the wavelength direction which samples the spectra just at the Nyquist criterion and minimizes read noise. The VIRUS-P field covers a $1'.6 \times 1'.6$ field with 246 fibers of $2''.05$ radius with a one-third fill-factor. We split our observations into three dithers to cover the entire field. In UGC 1281 we split our time further between two overlapping fields to cover the outer plane better in the presence of a possible <8° warp (García-Ruiz et al. 2002) yielding a total of six dithers. Spectrophotometric flux standard stars from Massey et al. (1988) were measured once or twice nightly. We tracked the transparency through the offset guiding camera. Galactic extinction corrections (Schlegel et al. 1998; O'Donnell 1994) were made with A_V=0.09 and A_V=0.15 for UGC 7321 and UGC 1281 respectively. A spectral airmass/extinction curve specifically modelled for the McDonald Observatory site was applied. We estimate its systematic uncertainty by comparing to the Kitt Peak curve supplied with the IRAF package `onedspec`. We find a 20% rms between the wavelengths of 6000-7000Å. The difference between the two curves deviates systematically at $\lambda > 5900$Å. We believe the site specific McDonald curve to be more accurate to our data. However, we propagate the difference as a potential, systematic uncertainty. The flux calibration uncertainty due to the airmass/extinction curve at the data's median airmass of 1.09 is $\pm$0.023 magnitudes.

3.1. Flux calibration

The $8'$ offset guiding camera is an Apogee Alta with a $20.25\square'$ field-of-view under a B+V (λ_{mean} = 5000Å) filter. Guider images were read out and saved every few seconds. Stacks of guider images that overlapped in time with each individual VIRUS-P exposure (20 minutes each
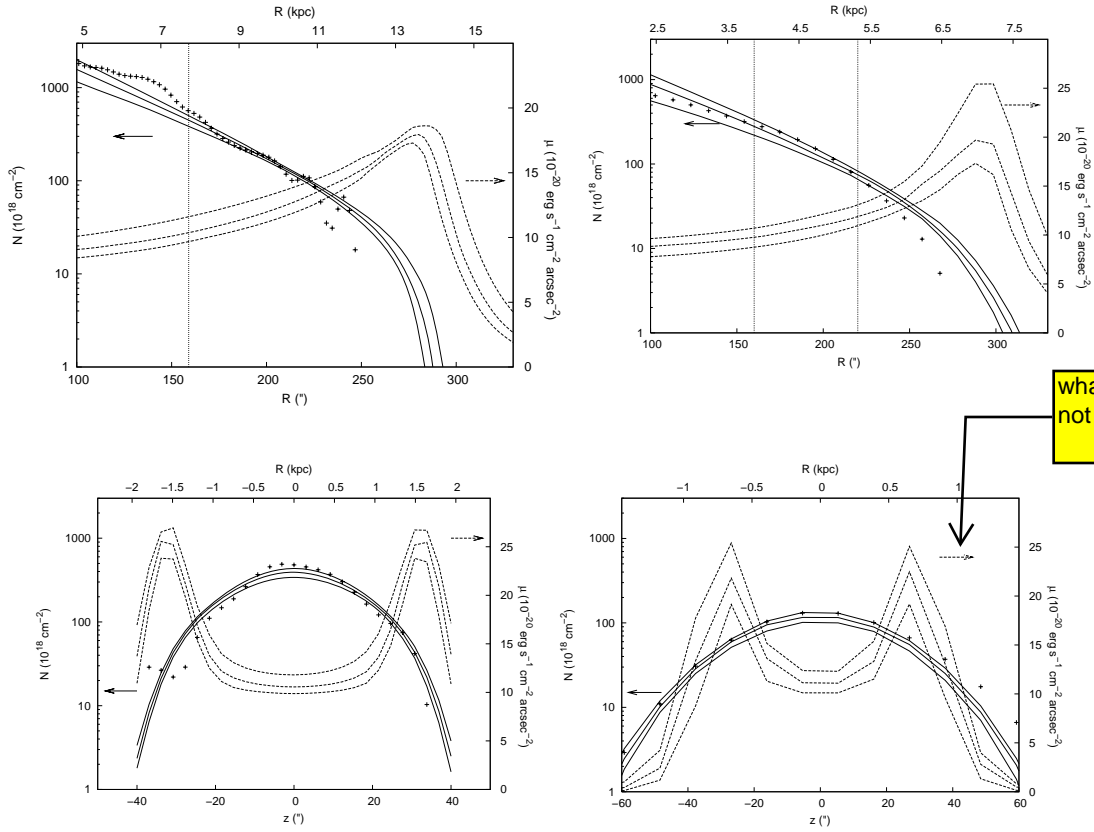
Fig. 2.— The single position angle, parameterized fits to the HI distributions. Because we use a single position angle and single radial scale length, the ranges over which we fit the HI distributions must be somewhat controlled and limited to the radii near the Hα observations. The smaller radii points not displayed in these plots begin to deviate from exponential distributions because of the loss of HI into H_2 or photoionization from the galaxies' centers and are not useful to our purpose. The predicted Hα surface brightness profiles are also shown against the right side axis. The stratification of Hα emission in these very thin galaxies is not captured in the model predictions of §2.2, but is captured in our preferred limit analysis of §2.1. The breaks at large radii in the 21 cm profiles are due to intersections with the photoionization fronts. *Top* The data along the major axes. *Bottom* The data along the minor axes at particular offsets. *Left* Cuts along the midplane and normal to it offset by 165″ with data, models, and 68% confidence intervals in UGC 7321. Since the disk may have a break in slope and a ≈ 3° warp exists, we restrict the fit to points > 160″ from the minor axis as indicated by the vertical dotted line. Using the best parameters from Table 1, the threshold radius (Equation 5) with the nominal value of $\Gamma = 4 \times 10^{-14}$ s^{-1} is predicted to be at $r_c = 13.4$kpc. Our spectroscopic data cover regions from R= 9.5kpc to R= 14.6kpc. *Right* Similarly, data and fits to UGC 1281. The offset here is 200″ from the minor axis. The points between the dotted lines at 160″ and 220″ form the restricted range of the fit as a ≈ 8° warp becomes important beyond. This fit appears poorer because of the larger warp, but a fit to all points at R > 220″ returns the same radial scale length to within the Monte Carlo errors. Using the best parameters from Table 1, the threshold radius (Equation 5) is predicted to be at $r_c = 7.4$kpc. Our spectroscopic data cover regions from R= 5.7kpc to R= 9.1kpc. Since we only show one dimensional cuts, these figures do not show all the datapoints used in the fits.

on UGC 1281, 30 minutes each on UGC 7321, and 1 minute each on the flux standards) were combined. We make a relative photometry correction to each science frame based on the stack of guider images taken simultaneously with the VIRUS-P data. Typically, ten stars per guider frame were available for photometry.

We have switched from the standard stars to the science targets with gaps of less than 5 minutes and assumed the conditions to be constant over that time and between the standard star and galaxy positions to make the absolute flux calibration. The observations of standard stars were taken during the most photometrically stable periods during each night to mitigate this potential source of error. Even so, the final flux calibration factor we apply may have systematic errors. We assess this error by considering the 5 observations of 2 standards, PG1708+602 and Feige 34, taken along with the UGC 7321 data and the 3 observations of 1 standard, Feige 110, taken along with the UGC 1281 data. The distribution in flux calibrations is wavelength-independent over our observed range with a 6.8% rms and 2.2% rms respectively. These estimates also capture possible variation in transparency with on-sky position. They are reported in Table 2 along with the possible error in the extinction curve between the guider effective wavelength and the wavelength of Hα. For the non-photometric data on UGC 7321, we measured a median zeropoint change, Δzp, of 0.276 magnitudes and a 68% range of 0.171-0.382 magnitudes over the two nights. The more nearly photometric data on UGC 1281 had median Δzp =0.057 magnitudes and a 68% range of 0.043-0.077 magnitudes over the three nights.

3.2. Sky background subtraction

The choice of sky subtraction is particularly important for this work which reaches for flux limits far below the average sky brightness. If the science field were covered with source emission, sky nods would be necessary. Then, the time variability of the OH and geocoronal Hα sky lines would form important systematic error sources. Fortunately, the large VIRUS-P field of view and selection of extremely thin, edge-on target galaxies affords a subset of fibers that contain a very small amount of source flux to serve as simultaneously measured sky fibers. We selected fibers sufficiently far from the major axis such that the models predicted $\mu < 2 \times 10^{-21}$ erg/s/cm^2/$\square''$(with the baseline $\Gamma = 4 \times 10^{-14}$ s^{-1}), or 100$\times$ below the expected peak surface brightness, to be used for sky subtraction. This cut left 24% and 44% of the fibers for sky estimation in UGC 7321 and UGC 1281 respectively. We experimented with moving this sky fiber cut up and down by a factor of five and found no difference in the final upper limits to the UVB strength. Depending on the number of fibers co-added, the statistical Hα flux errors presented here reach to 300$\times$ dimmer than the sky level. Without simultaneously measured sky background, the systematics of sky nods would quickly dominate the limits.

3.3. Data reduction

The data reduction, optimal background subtraction, and emission line detections were completed with algorithms developed for a Lyman-α emitter survey (Adams et al., 2010, ~~in prep.~~). We summarize here the important steps. First, overscans and a master bias frame are subtracted from each frame. The wavelength solution for each fiber is fit as a fourth order polynomial to ~ 30 emission lines from HgCd lamps passing through the entire telescope light path. The residuals to the solution are of order one hundredth of a resolution element. Flat fields precise to $< 1\%$ are made from twilight flats with the solar spectrum removed by a b-spline fit (Dierckx 1993) and division. This fit method is the same as we apply to fitting and subtracting the sky background and has important advantages over data interpolation. By avoiding data resampling, we keep the errors uncorrelated. Small distortions of the instrument camera over a regular pixel grid lead to the spectrum from each fiber being sampled at slightly different wavelengths. By considering a collection of fibers together in a fit, the spectrum is oversampled, and we can recover nearly blended features. This method delivers an optimal spectral model robust against cosmic rays and without the residuals that linear interpolation can create. A thorough description of b-spline fits as applied to astronomy datasets can be found in Kelson (2003). The next step in the data reduction is to fit and subtract a b-spline sky background modelled from selected sky fibers. Next, cosmic rays are masked by finding all pixels that deviate from the other pixels in the same fiber by some large threshold value. Some dim cosmic rays are missed by this step, but are rejected when combining multiple frames. We have chosen a threshold that misses the weakest $\sim$20% of cosmic rays for direct masking in this work. The exact threshold does not affect the results. The frame is then flux calibrated with the non-photometric zeropoint correction and airmass correction applied. Finally, a one dimensional final spectrum for each fiber position is created by combining all the frames taken at the same dither position and running across the 5 pixel cross-dispersion aperture. For the final estimate to be immune to remaining cosmic rays we have used the biweight estimator (Beers et al. 1990) at this step. Our pipeline makes no cross-talk correction since we restrict our cross-dispersion apertures to 5 pixels where the fiber separations are typically 8 pixels and the cross-dispersion FWHMs are typically 4 pixels. This leads to, at most, 10% contamination from neighboring fibers and becomes especially trivial when considering large collections of fibers as an aperture. The scattered light properties of the instrument have been characterized in Adams et al. (2008) and, particularly at Hα wavelengths, no scattered light or ghost patterns are found. The spectral resolution varies by $< 5\%$ for all fibers at a common wavelength due to careful design and alignment of the spectrograph camera. We have made no corrections by convolution to a common resolution. The effect of the spectral resolution variation and the backgrounds subtraction scheme is to leave residuals under bright skylines. We characterize the spectral resolution systematic in §3.5. Given the large number of independent spectral elements in VIRUS-P data (126,000 in each dither), we must choose a high significance cut. At 5σ significance, the chance of noise leading to a detection at a particular wavelength in a particular dither is only 1 in 14,000. We choose to quote this limit as sufficiently conservative.

3.4. Emission line detection

We describe here an automated emission line search algorithm to work with a sky background and continuum subtracted spectrum or stacks of spectra. By applying this search, we robustly find all significant emission lines at all redshifts. In practice, we find no significant Hα emission with plausible velocity offsets in any fiber for either galaxy. Plausible velocity offsets are determined by the HI rotation curves. In UGC 7321, for example, the rotation curve is flat over our data range with variations of only ±10 km s^{-1}. The gas dispersion in unmeasured in the HI data, but presumed to be near 7 km s^{-1} (Uson & Matthews 2003). Over a very conservative ±100 km s^{-1} (2.2Å) range around our target wavelengths, the flux limit is flat. First, spectral pixels at any wavelength that exceed the noise by 1σ are treated as seeds. Around each seed, we fit Gaussian profiles of variable intensity, width, and central wavelength. The S/N of an emission line is then calculated by summing all pixels and errors in quadrature within $\pm2\sigma_{res}$ for the wavelength of interest where σ_{res} is the instrumental dispersion. In the UGC 7321 data, $\sigma_{res} =33$ km s^{-1}, and in the UGC 1821 data, $\sigma_{res} =100$ km s^{-1}. When quoting limits on undetected emission lines, we sum in quadrature the errors within the same spectral window. These steps in error combination consider both the statistical errors in the reduced data and the systematic error based on ill-matched spectral resolution between fibers discussed in §3.6. A spectral correction factor is divided into the detections and limits to consider the fraction of a Gaussian function's flux that falls outside of the considered window as $f_{spec} = \mathrm{erf}(\sqrt{2}\sigma_{res}/\sqrt{\sigma_{res}^2 + \sigma_{det}^2})$ where σ_{det} is the detected emission line width. This same factor determines the degradation in flux limit for broad line detections. For unresolved limits, σ_{det} is considered to be zero and the spectral correction (f_{spec}^{-1}) evaluates as $\times1.05$. In practice, we make no significant detections within ±500 km/s of the HI based expected velocity in either galaxy. The average HI heliocentric velocities of UGC 7321 and UGC 1281 are 407 km/s (Uson & Matthews 2003) and 157 km/s (García-Ruiz et al. 2002) with the asymptotic HI velocities nearest our pointings at $\sim$510 km/s and $\sim$210 km/s respectively. We observed under topocentric radial velocities of -12 km/s and 3 km/s toward UGC 7321 and UGC 1281 respectively. Therefore, we expect unresolved Hα emission at 6573.7$\pm$0.4Å and 6567.5$\pm$0.8Å using the asymptotic values just quoted, in the observed frames of UGC 7321 and UGC 1281 respectively. The gas dispersions are unresolved in the 21 cm data, but believed to be of order 7 km s^{-1}. The 21 cm rotation curves change by ±10 km s^{-1} over our fields. These two values form the expected wavelength range, and in comparison the flux limits around these lines are flat to ±100 km s^{-1}.

Background galaxies produce the dominant flux in a number of fibers. This is evident where we can measure redshifts through emission lines identifiable as either Lyman-α, [OII]$\lambda3727$, Hβ, [OIII]$\lambda4959$, or [OIII]$\lambda5007$. For most of the background systems with emission lines the redshift is determined by the pattern of multiple emission lines. If the background galaxies have smooth continuum through our wavelength of interest their removal is accomplished in the continuum removal step. However, the possibility of continuum structure across the Hα wavelength ranges leads us to mask those regions. Operationally, we mask a fiber if it displays a 5σ significant value in its continuum as estimated across all available wavelengths under inverse variance weighting.

It is also possible that weak continuum is coming from objects in the halo of the target galaxies, in which case the desirability of a mask is less certain. We have performed all the emission line searches and limits with and without a masking process and found no detections in either case. The values we present as limits were made with the masks applied.

3.5. Data stacks and limits

We show the derived limits in Table 2. We find no significant emission lines within the vicinity of the galaxies' velocities (defined as within ± 500 km s^{-1}) in any individual fiber. We next mask out continuum sources and apply a circular spatial filter as a 2D Gaussian function kernel with FWHM=10$''$. Again, we find no significant emission. Finally, we stack all fibers which by the model should have $\mu > 10^{-19}$ erg/s/cm^2/$\square''$. The models used to select those fibers are those presented in Table 1 with an assumed $\Gamma = 4 \times 10^{-14}$ s^{-1} and $\beta = 1.8$. We use the nearly linear scaling between Γ and μ to determine the true value of Γ. The models predict such averages to yield 1.7×10^{-19} erg/s/cm^2/$\square''$ for UGC 7321 and 1.8×10^{-19} erg/s/cm^2/$\square''$ for UGC 1281. We again find no significant emission in the stacked spectra. These emission line searches were performed solely with the Poisson errors and yielded no detections. In §3.6 we discuss additional systematic errors that degrade the final limits further and also yield no significant emission line detections. By the models, the peak Hα surface brightness would have fallen in our fields for UVB strengths from 2×10^{-14} s$^{-1} < \Gamma < 2 \times 10^{-12}$ s^{-1} and warps of $<12.4°$ in UGC 7321 and 4×10^{-15} s$^{-1} < \Gamma < 3 \times 10^{-13}$ s^{-1} and warps of $<15.8°$ in UGC 1281. However, a radial displacement of the field would still give significant flux as seen in the contour plots, so we do not expect misalignments to affect the final limits. We show in Figure 4 the sky spectra and the three types of spectral stacks to background subtracted data in UGC 7321. In Figure 5 we show the same for UGC 1281. In neither case do we make a significant detection in Hα.

3.6. Error assessment

There are several potential sources of systematic error to the presented spectra. We have already discussed the uncertainties in the model-based conversion of Hα surface brightness to UVB strength in §2.3. The uncertainty in the absolute spectral flux calibration due to the applied atmospheric extinction curve is discussed in §3. The uncertainty in the absolute spectral flux calibration due to the standard star observations is discussed in §3.1. We now analyze a final systematic regarding the relative error determinations in the Hα spectra. We observe that the propagation of the errors from the data's original read noise and shot noise does not fully account for the variation in sky subtracted spectra. This is especially true under bright skylines. We discuss three possible causes with a focus on the variation of spectral resolution across different fibers. In any of the cases, the form of the systematic error will be a small fraction multiple of the continuum subtracted sky background spectrum.

Table 1. HI based model parameters and Hα surface brightness predictions*

Galaxy	n_0 (cm^{-3})	h_z (pc)	h_r (kpc)	i (°)	PA (°)	μ_0 †	$(\mu \otimes S)_0$ ‡	$\bar{\mu}$ ††	μ_{AR} **
UGC 7321	$3.3^{+3.5}_{-1.7}$	$426.^{+120.}_{-88.} d_{10}$	$2.12^{+0.25}_{-0.16} d_{10}$	$82.8^{+0.9}_{-0.6}$	-100.1 ± 0.1	$18.4^{+1.0}_{-0.9}$	$16.7^{+1.1}_{-0.7}$	$16.6^{+1.0}_{-0.3}$	$22.8^{+4.4}_{-1.8}$
UGC 1281	$3.8^{+3.2}_{-2.6}$	$303.^{+70.}_{-58.} d_5$	$1.17^{+0.19}_{-0.14} d_5$	$84.9^{+4.0}_{-1.3}$	-141.3 ± 0.3	$21.4^{+12.1}_{-2.8}$	$19.4^{+5.6}_{-2.4}$	$17.9^{+1.7}_{-1.1}$	..

*Fit under the restricted radial ranges per Figure 2 and with $\Gamma = 4 \times 10^{-14}$ s^{-1} and $\beta = 1.8$ assumed.

†10^{-20} erg/s/cm^2/□″

‡10^{-20} erg/s/cm^2/□″, smoothed by a circular 10″ FWHM kernel

††10^{-20} erg/s/cm^2/□″, average for all fiber positions with $\mu > 10^{-19}$ erg/s/cm^2/□″

**10^{-20} erg/s/cm^2/□″, based on disk's projected aspect ratio (Equations 6-8 of Weymann et al. (2001))

HI bound?

Table 2. Error budget and limits to the UVB strength

Co-addition type (1)	Poisson error (2)	Resolution systematic (3)	Flux calibration (4,%)	SB upper limit (5)	Model systematic (6,%)	$\Gamma(z=0)$ upper limit (7)	χ^2/ν (8)
UGC 7321 each single fiber	11.0	0.8	8.9	64	+5.4/-4.9	15	353/468
UGC 7321 smoothed	2.8	0.4	8.9	17	+6.6/-4.2	4.4	257/454
UGC 7321 radio bound stack	1.8	0.4	8.9	12	+19.3/-7.9	2.3	545/462
UGC 7321 full stack	0.9	0.4	8.9	7.1	+6.0/-1.8	1.7	497/454
UGC 1281 each single fiber	18.6	29.5	4.3	250	+57/-13	53	68/136
UGC 1281 smoothed	6.6	8.9	4.3	81	+29/-12	19	218/136
UGC 1281 full stack	2.0	8.9	4.3	57	+9.5/-6.1	14	50/134

$^{(1)}$Detection and model method. Smoothed refers to a 10″ FWHM circular kernel.

$^{(2)}$1σ (10^{-20} erg/s/cm^2/□″) in the spectral data from Poisson noise.

$^{(3)}$1σ (10^{-20} erg/s/cm^2/□″) in the spectral data from spectral resolution or sky line variation. See §3.6.

$^{(4)}$1σ (%) flux calibration systematic including 2.1% for airmass/extinction error.

$^{(5)}$5σ (10^{-20} erg/s/cm^2/□″) limit in surface brightness.

$^{(6)}$1σ (%) model surface brightness systematic.

$^{(7)}$5σ (10^{-14} s^{-1}) total limit assuming $\beta = 1.8$. The achieved Hα surface brightness limit is compared to the low bound of the modeled Hα surface brightness to create this final, linearized estimate from the modeled value of $\Gamma 4 \times 10^{-14}$ s^{-1}.

$^{(8)}\chi^2$ of all pixels between 6300-6600Å in the spectrum and the degrees of freedom.
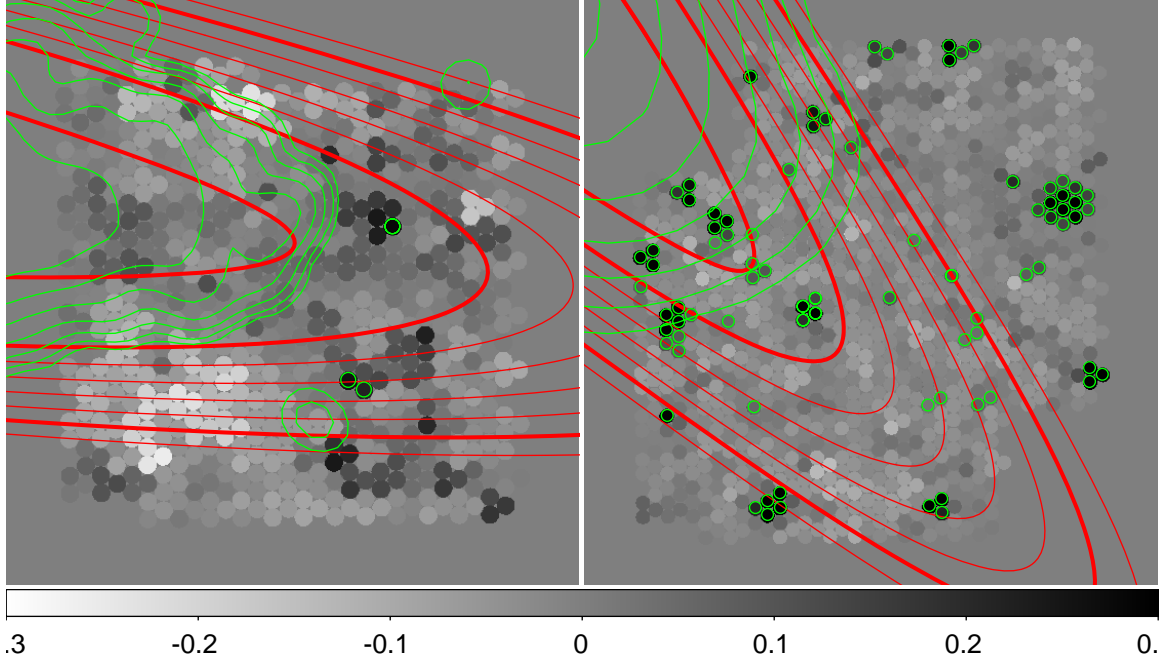
Fig. 3.— *Left* Reconstructed VIRUS-P continuum image of the UGC 7321 outskirts centered at α_{J2000}=12:17:16.4 and δ_{J2000}=+22:31:33 or $\approx$250″ off the minor axis. The continuum estimation is made through the entire available spectral range from 6040-6740Å with the colorbar in units of 10^{-17} erg s^{-1} cm^{-2} Å^{-1}. The dark, circled objects are masked as background galaxies, many known to be background by their emission lines at redshifts higher than the target galaxy's redshift. One can see some broad structure in the continuum map due to small residuals in the fiber-to-fiber throughput, especially in the UGC 7321 data. The green contours trace the HI column densities in steps of (10,19,36,67,126,238,448,845) $\times 10^{18}$ cm^{-2}. The red, more extended contours trace the predicted Hα surface brightness assuming $\Gamma = 4 \times 10^{-14}$ s^{-1} and $\beta = 1.8$ in contour levels of (0.1,0.24,0.57,1.4,3.3,7.9,19) $\times 10^{-20}$ erg/s/cm^2/$\square$″. The two innermost red contours enclose the surface brightness maxima. Positions closer to the center again become dimmer in Hα since portions of the gas, in projection, stay neutral at smaller radii. The fibers used in sky subtraction are all those outside the second outermost red contour. We draw the second, seventh, and eighth contours thickly to highlight these regions. As a scale reference, the fiber diameter is 4″.1. *Right* The same display for UGC 1281 with central position α_{J2000}=1:49:15.8 and δ_{J2000}=+32:31:46 or ≈ 300″ off the minor axis. The continuum estimation is made through the entire available spectral range from 4700-6990Å. Here, many more background galaxies are found. In UGC 1281, we took data at two overlapping fields. The central positions covered by both square pointings have the best depth.
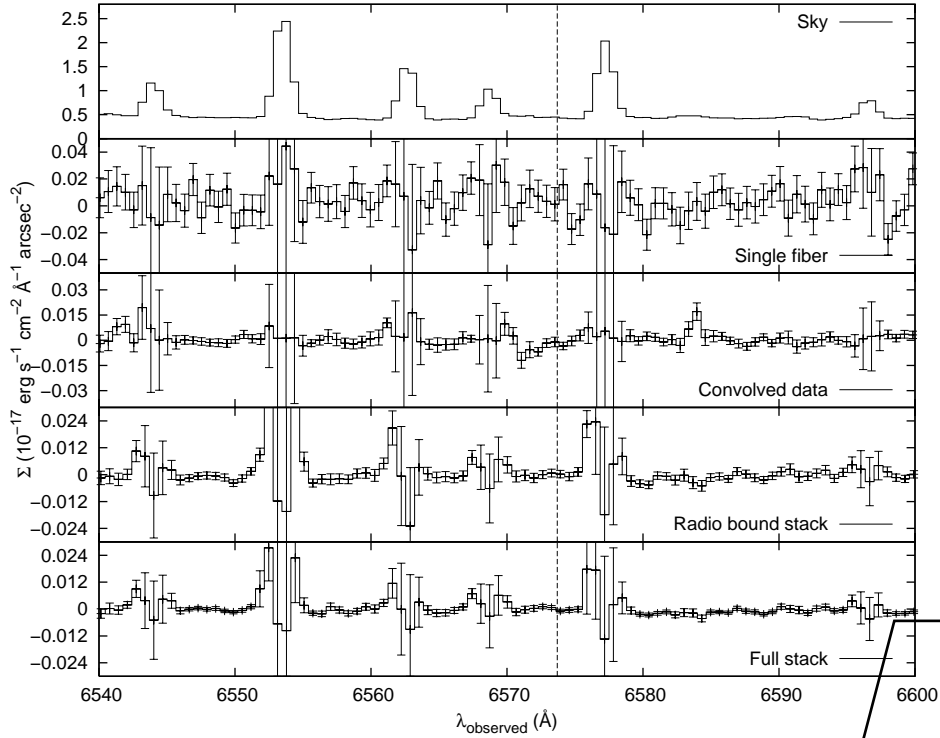
Fig. 4.— Selected spectra around Hα in UGC 7321 presented in units of surface brightness. The expected wavelength for emission is shown with a dotted line. The frames from top to bottom show the background sky, the background subtracted spectrum for a particular fiber that does not display continuum, the spectrum at the same position after being smoothed by a 10″ FWHM circular Gaussian kernel, and finally the stack of the 358 fibers predicted to be the brightest by the model. The errorbars consist of the Poisson, observational error and the systematic spectral resolution error of columns two and three in Table 2 only. The spectral resolution systematic, dicussed in §3.6, is most important under the bright skylines and does not dominate at the target wavelength.

First, the instrumental spectral resolution varies by at most 5% in different fibers due to small but detectable optical distortions in the camera. We further measure from arc lamp exposures that the variation is 2.5% between the sky and science fibers in the UGC 7321 data and 1.5% in the UGC 1281 data. These factors are presented in column 3 of Table 2 and scaled by the background subtracted sky spectrum and applied as systematic errors to Figures 4 and 5. This form of the systematic, as the fractional error in the dispersion times the background subtracted sky spectrum, can be derived simply by taking the first order expansion of a Gaussian function near the line center. Second, the fiber-to-fiber throughput can vary slightly between flat field calibrations. The relative fiber-to-fiber throughput is calibrated with sky flats taken in dawn and dusk. This relative throughput has been measured to be stable to <5% over most nights. However, we find a maximum 15% fiber-to-fiber throughput variation in the UGC 7321 data due to poor fiber cable coiling practices. This error is very evident in the broadband estimate per fiber as shown in Figure 3. The error is less important for a continuum subtracted spectral element where most of the fiber-to-fiber throughput error subtracts out. The form of the throughput variation is that a few fibers experience a change with time, but the majority stay stable. We measure the rms throughput variation between all fibers to be far below 1%. Third, sky lines may vary across the $\sim 1'$ separating the sky and science fibers. The UGC 7321 data is well resolved from all known sky lines and only near OH lines, but the UGC 1281 data is unresolved from an OH line and near the geocoronal Hα. Such variations have not been observed, and the data are averaged over very long integration times and large ranges in zenith distance, so we do not expect them to be a dominant error term. It is possible that the geocoronal Hα emission may vary within $\sim 1'$, but small-scale variation is less likely for OH. We choose to parameterize the total effect of these systematics in a conversative manner by deriving the systematic error based on the measured levels of spectral resolution variation seen between fibers.

This systematic error strongly affects the UGC 1281 data since the lower resolution allows blending of night sky lines at the expected wavelength of Hα, but it is a more minor component to the UGC 7321 error budget. As data from more fibers are coadded, this systematic error takes on greater importance in relation to the random error. We assess the χ^2 distributions across 6300-6600Å in each co-addition case in Table 2. The χ^2 are simply calculated against a flat, zero flux line and can be visually judged in Figures 4 and 5. The distributions look very symmetric around zero, and the reduced χ^2 values are consistent with noise. The proper χ^2 values validate our systematic noise estimates empirically. In fact, the additional noise estimates may be slightly conservative. One can visually note from Figures 4 and 5 that the χ^2 values are even lower than the degrees of freedom (ν) in the most important regions near the target wavelengths.

3.7. Internal galactic extinctions

The internal extinctions in disk galaxies at these scale lengths are very uncertain despite being a subject of detailed research (e.g. Byun et al. 1994). Matthews et al. (1999) see in UGC 7321 an

abrupt truncation of resolved dust clumps beyond r$\approx$80$''$ and fit a model of radially declining dust where, for our position around 250$''$, there is no internal extinction. We have taken short VIRUS-P exposures covering Hα and Hβ on the galaxy centers to derive conversative internal extinction upper limit estimates after correction for Galactic extinction. We did not take deep enough exposures to ourselves measure accurate stellar populations and photospheric Balmer absorptions, so we have relied on literature values appropriate to late type galaxies. From the Balmer decrements we measure A$_{H\alpha}$=-0.03±0.09 magnitudes for UGC 7321 and A$_{H\alpha}$=-0.02±0.11 magnitudes for UGC 1281 under the assumption that the absorption equivalent widths satisfy EW(Hα)$_{abs}$=EW(Hβ)$_{abs}$=2Å (McCall et al. 1985; Calzetti et al. 1994). As the extinction estimates are consistent with zero, we apply no dust correction to our results.

4.   Discussion

The flux decrement method is currently the most widely used method to estimate the UVB strength at high redshift. Under the fluctuating Gunn-Peterson approximation (Croft et al. 1998), the Lyman-α forest optical depth distribution should have a normalization that depends only on well constrainted cosmological parameters and the UVB strength. The IGM temperature and density distributions may have some systematic uncertainties that propagate into knowledge of the UVB, but they are not likely the leading uncertainties. The more likely dominant uncertainties in flux decrement modeling are the source emissivities. At $z \lesssim 1$, the Lyman limit mean free path becomes larger than the horizon, so the UVB strength at z=0 is influenced by source evolution across this redshift range. AGN and stellar population luminosity functions, both observed and modeled, generally agree to better than an order of magnitude over these redshifts. The least constrained input to flux decrement modeling is the escape fraction for ionizing photons in galaxies, particularly at low redshift and low luminosity. We believe our measurement is best interpreted as an indicator of a low escape fraction.

Our most constraining (5σ) spectral limits are $\Gamma < 1.7 \times 10^{-14}$ s^{-1} in UGC 7321 and $\Gamma < 13.5 \times 10^{-14}$ s^{-1} in UGC 1281 again assuming $\beta = 1.8$. Several benchmarks, both empirical and theoretical, exist with which to compare these limits. Figure 6 shows the UVB strength against redshift determined by many groups. The lowest redshift proximity effect measurement comes from Kulkarni & Fall (1993) with analysis of 13 quasars from Bahcall et al. (1993) between $0.16 \leq z \leq 1.00$ at $\Gamma(\bar{z} = 0.5) = 2.0^{+10}_{-1.3} \times 10^{-14}$ s^{-1}. However, the proximity effect method has been shown to have a high bias that depends on halo mass (Faucher-Giguère et al. 2008c) and should be interpreted with care. The theoretical model of Faucher-Giguère et al. (2009) gives a drop in the UVB strength by a factor of 3.4 between z=0.5 and z=0.0 leaving this measurement consistent with our current limit. This agreement is interesting and somewhat unexpected given the bias of proximity effect measurements. The only existing low-z flux decrement measurement is $\Gamma(\bar{z} = 0.17) = 5.0^{+20}_{-4.0} \times 10^{-14}$ s^{-1} (Davé & Tripp 2001). The theoretical model itself, normalized by the flux decrement method, predicts $\Gamma(z = 0) = 3.8 \times 10^{-14}$ s^{-1} which is much higher than our new

limit. There exists a second set of unpublished theoretical predictions from F. Haardt and P. Madau discussed in Faucher-Giguère et al. (2009) giving $\Gamma(z=0) = 1 \times 10^{-13}$ s^{-1}. The latter model used a constant 10% escape fraction of ionizing photons and an unspecified star formation history while the former used a completely theoretical and simulation-based star formation history (Hernquist & Springel 2003) and a scaling of the stellar UV emissivity based on high redshift flux decrement measurements that contains the escape fraction. A comparison to Lyman-break galaxy (LBG) luminosity functions led that group to require only $f_{esc,abs} \approx 0.5\%$ (Faucher-Giguère et al. 2008b). The direct measurement of galactic escape fractions is difficult due to the low values involved. While UV bright samples can range up to $\approx 3\%$ in absolute Lyman limit escape fraction (Shapley et al. 2006), a presumably lower-mass sample yielded $(2\pm2)\%$ (Chen et al. 2007). Theoretical work shows a strong decrease in f_{esc} with star formation rate and halo mass (Gnedin et al. 2008) below $M_{tot} \approx 10^{11} M_\odot$, and lower redshift observations of populations similar to LBGs show a potential redshift evolution (Siana et al. 2010) with $f_{esc,abs} < 0.8\%$. There is no reason yet to suppose a lower bound to the escape fraction. If we interpret our limit as a scaling of the escape fraction from the models in Faucher-Giguère et al. (2008b) at low redshift, we find $f_{esc,abs} < 0.2\%$.

It is unlikely the systematics of poor assumptions in our measurements can cause the disagreement. Contaminating ionization from the galaxies' forming stars would bias our measurement high, only making the disagreement more severe. We further note that the degree of contamination can be measured by anomalous [NII]$\lambda6548$ to Hα ratios (BFQ) and should not, in principle, limit this type of measurement. There has been a large body of work on low strength star formation beyond the optical radii in local galaxy disks, usually labelled extended UV disks (XUV), fostered by far UV (FUV,1350-1750Å) and near UV (1750-2750Å) Galaxy Evolution Explorer (GALEX) data (e.g. Thilker et al. 2007). Narrowband Hα imaging and spectroscopy has revealed that $\sim 10\%$ of gas rich disks (Werk et al. 2010a,b; Herbert-Fort et al. 2010) host outlying Hα emitting complexes as either compact HII regions or dwarf satellite companions. The common Hα fluxes observed so far are of the order of a few times 10^{-16} erg/s/cm^2. Any such systems would have been found in our data as strong detections limited in size to a few fibers. The expectation of large-scale, diffuse UVB Hα emission should reliably discriminate against compact XUV Hα emission. We have also visually inspected the target galaxies' GALEX data which have not yet been analyzed in any XUV focused work. UGC 1281 has only been covered in the rather shallow all-sky survey mode. UGC 7321 has been covered for 2.8ks in the NUV and 1.7 ks in the FUV under guest investigator cycle 4 proposal ID 095 (PI: J. Lee) as part of the 11HUGS project (Lee et al. 2009). In neither system is there evidence for an extended UV disk beyond the DSS2-red[2] limiting contours. Finally, these contamination issues are speculative until a putative UVB Hα detection is made. The only possible systematics that could have made a low bias to our limit are unaccounted for dust or gas

---

[2]The Digitized Sky Survey was produced at the Space Telescope Science Institute under U.S. Government grant NAG W-2166. The images of these surveys are based on photographic data obtained using the Oschin Schmidt Telescope on Palomar Mountain and the UK Schmidt Telescope. The plates were processed into the present compressed digital form with the permission of these institutions.

distribution parameters, such as inclination, far beyond the range we have constrained. We have made our principal analysis under the assumption that the gas distribution extends beyond the HI data limits with the same exponential form as at smaller radii. This assumption, motivated by the thin and regular HI distributions and lack of nearby companions, has the strongest impact on our interpretation. A weaker estimate without this assumption yields $\Gamma < 2.3 \times 10^{-14}$ s^{-1} at 5σ significance in UGC 7321. This result raises the question whether a redshift-dependent escape fraction exists or whether the UVB strength has been overestimated at all redshifts, in disagreement with flux decrement measurements. The latter choice would upset the apparent agreement between current models and reionization constraints. Either case will require some modification to the UVB strength model and its implementation in structure formation simulations. We intend to pursue our measurements of these and other superthin galaxies to greater depth in order to arrive at a detection of $\Gamma(z = 0)$.

A. Full solution to the general Hα surface brightness

We give here the derivation of the general Hα surface brightness at field positions b_1 and b_2. The special case for $b_1=r_c$ and $b_2=0$ was derived as Equation 9. That case is simplified since the line of sight integration can proceed from zero to infinity without intersecting the photoionization boundary and has symmetry between positive and negative values of ρ. For the general case, the simple task presented in this Appendix is to find the possible geometrical intersections of z from Equation 7 and $z_c(R)$ from Equation 6 as a function of ρ under inputs i, b_1, and b_2. This may have zero or two intersections labelled as ρ_{r1} and ρ_{r2}. Once found, the general expression for μ then follows Equation A1.

$$\mu(b_1, b_2) = \frac{\chi^2 \varepsilon^2 \alpha_{H\alpha}^{eff} n_0^2 h \nu_{H\alpha} \gamma}{\Omega}$$

$$\text{with } \gamma = \begin{cases} \int_{-\infty}^{\infty} \exp\left(-\frac{2\rho\cos i}{h_z} - \frac{2\sqrt{r_c^2+\rho^2\sin^2 i}}{h_r}\right)d\rho & : \text{no roots in } \rho \\ \int_{-\infty}^{\rho_{r1}} \exp\left(-\frac{2\rho\cos i}{h_z} - \frac{2\sqrt{r_c^2+\rho^2\sin^2 i}}{h_r}\right)d\rho + \\ \int_{\rho_{r2}}^{\infty} \exp\left(-\frac{2\rho\cos i}{h_z} - \frac{2\sqrt{r_c^2+\rho^2\sin^2 i}}{h_r}\right)d\rho & : \text{roots in } \rho \end{cases} \tag{A1}$$

The first necessary condition for any intersection to occur is evidently expressed in Equation A2, as the largest possible distance for an intersection to lie from the galaxy center is r_c while the closest possible approach for a sight line is b_1.

$$b_1 < r_c \tag{A2}$$

The intersections in ρ can be expanded into simple quadratic equations. Each of the two potential roots from the quadratic solution is double valued when considering intersections with both signs of the $z_c(R)$ surface leading to four possible roots. However, only at most two of the roots will be physical with the rejected two lying on extrapolations of $z_c(R)$ at $R(\rho) > r_c$ or $|z(\rho)| > r_c \times h_z/h_r$. The intersections with these surfaces lead to possible limits ρ_{s1}, ρ_{s2}, ρ_{s3}, and ρ_{s4} expressed in Equations A3-A6. The most constraining limits are then the values between these four with the smallest absolute values leading to Equations A7-A8 for the active limits ρ_{l1} and ρ_{l2}.

$$\rho_{s1} = \frac{-b_2 \sin i - \frac{h_z}{h_r} r_c}{\cos i} \tag{A3}$$

$$\rho_{s2} = \frac{b_2 \cos i - \sqrt{r_c^2 - b_1^2}}{\sin i} \tag{A4}$$

$$\rho_{s3} = \frac{-b_2 \sin i + \frac{h_z}{h_r} r_c}{\cos i} \tag{A5}$$

$$\rho_{s4} = \frac{b_2 \cos i + \sqrt{r_c^2 - b_1^2}}{\sin i} \tag{A6}$$

$$\rho_{l1} = \max(\rho_{s1}, \rho_{s2}) \tag{A7}$$

$$\rho_{l2} = \min(\rho_{s3}, \rho_{s4}) \tag{A8}$$

The potential intersections with $z_c(R)$ can be directly evaluated as ρ_{p1}, ρ_{p2}, ρ_{p3}, and ρ_{p4} as given in Equations A9-A12.

$$\rho_{p1} = \frac{\left(\frac{h_r}{h_z}\right) r_c \cos i - \left(\frac{h_r}{h_z}\right)^2 b_2 \sin i \cos i - b_2 \sin i \cos i + \sqrt{\beta_{p1}}}{\left(\frac{h_r}{h_z}\right)^2 \cos^2 i - \sin^2 i}$$

$$\beta_{p1} = 2\left(\frac{h_r}{h_z}\right)^2 b_2^2 \cos^2 i \sin^2 i - 2\left(\frac{h_r}{h_z}\right) b_2 r_c \cos^2 i \sin i + b_1^2 \left(\frac{h_r}{h_z}\right)^2 \cos^2 i$$

$$+ b_2^2 \left(\frac{h_r}{h_z}\right)^2 \sin^2 i + r_c^2 \sin^2 i + \left(\frac{h_r}{h_z}\right)^2 b_2^2 \sin^4 i - 2\left(\frac{h_r}{h_z}\right) r_c b_2 \sin^3 i - b_1^2 \sin^2 i \tag{A9}$$

$$\rho_{p2} = \frac{\left(\frac{h_r}{h_z}\right) r_c \cos i - \left(\frac{h_r}{h_z}\right)^2 b_2 \sin i \cos i - b_2 \sin i \cos i - \sqrt{\beta_{p1}}}{\left(\frac{h_r}{h_z}\right)^2 \cos^2 i - \sin^2 i}$$

$$\beta_{p1} = 2\left(\frac{h_r}{h_z}\right)^2 b_2^2 \cos^2 i \sin^2 i - 2\left(\frac{h_r}{h_z}\right) b_2 r_c \cos^2 i \sin i + b_1^2 \left(\frac{h_r}{h_z}\right)^2 \cos^2 i$$

$$+ b_2^2 \left(\frac{h_r}{h_z}\right)^2 \sin^2 i + r_c^2 \sin^2 i + \left(\frac{h_r}{h_z}\right)^2 b_2^2 \sin^4 i - 2\left(\frac{h_r}{h_z}\right) r_c b_2 \sin^3 i - b_1^2 \sin^2 i \tag{A10}$$

$$\rho_{p3} = -\frac{\left(\frac{h_r}{h_z}\right) r_c \cos i - \left(\frac{h_r}{h_z}\right)^2 b_2 \sin i \cos i - b_2 \sin i \cos i + \sqrt{\beta_{p2}}}{\left(\frac{h_r}{h_z}\right)^2 \cos^2 i - \sin^2 i}$$

$$\beta_{p2} = 2\left(\frac{h_r}{h_z}\right)^2 b_2^2 \cos^2 i \sin^2 i + 2\left(\frac{h_r}{h_z}\right) b_2 r_c \cos^2 i \sin i + b_1^2 \left(\frac{h_r}{h_z}\right)^2 \cos^2 i$$

$$+ b_2^2 \left(\frac{h_r}{h_z}\right)^2 \sin^2 i + r_c^2 \sin^2 i + \left(\frac{h_r}{h_z}\right)^2 b_2^2 \sin^4 i + 2\left(\frac{h_r}{h_z}\right) r_c b_2 \sin^3 i - b_1^2 \sin^2 i \qquad \text{(A11)}$$

$$\rho_{p4} = -\frac{\left(\frac{h_r}{h_z}\right) r_c \cos i - \left(\frac{h_r}{h_z}\right)^2 b_2 \sin i \cos i - b_2 \sin i \cos i - \sqrt{\beta_{p2}}}{\left(\frac{h_r}{h_z}\right)^2 \cos^2 i - \sin^2 i}$$

$$\beta_{p2} = 2\left(\frac{h_r}{h_z}\right)^2 b_2^2 \cos^2 i \sin^2 i + 2\left(\frac{h_r}{h_z}\right) b_2 r_c \cos^2 i \sin i + b_1^2 \left(\frac{h_r}{h_z}\right)^2 \cos^2 i$$

$$+ b_2^2 \left(\frac{h_r}{h_z}\right)^2 \sin^2 i + r_c^2 \sin^2 i + \left(\frac{h_r}{h_z}\right)^2 b_2^2 \sin^4 i + 2\left(\frac{h_r}{h_z}\right) r_c b_2 \sin^3 i - b_1^2 \sin^2 i \qquad \text{(A12)}$$

The comparisons to the limits ρ_{l1} and ρ_{l2} discard unphysical values in Equations A13-A14 where the final limits of integration are found.

$$\rho_{r1} = \min(x \in \{\rho_{p1}, \rho_{p2}, \rho_{p3}, \rho_{p4}\} : \rho_{l1} < x < \rho_{l2}\}) \qquad \text{(A13)}$$

$$\rho_{r2} = \max(x \in \{\rho_{p1}, \rho_{p2}, \rho_{p3}, \rho_{p4}\} : \rho_{l1} < x < \rho_{l2}\}) \qquad \text{(A14)}$$

With the integration boundaries now well defined, $\mu(b_1, b_2)$ can easily be obtained through numerical integration.

REFERENCES

Adams, J. J., Hill, G. J., & MacQueen, P. J. 2008, in Proc. SPIE, Vol. 7014, 232

Bahcall, J. N., Bergeron, J., Boksenberg, A., Hartig, G. F., Jannuzi, B. T., Kirhakos, S., Sargent, W. L. W., Savage, B. D., Schneider, D. P., Turnshek, D. A., Weymann, R. J., & Wolfe, A. M. 1993, ApJS, 87, 1

Bajtlik, S., Duncan, R. C., & Ostriker, J. P. 1988, ApJ, 327, 570

Beers, T. C., Flynn, K., & Gebhardt, K. 1990, AJ, 100, 32

Bland-Hawthorn, J., Freeman, K. C., & Quinn, P. J. 1997, ApJ, 490, 143

Bochkarev, N. G., & Sunyaev, R. A. 1977, AZh, 54, 957

Bouwens, R. J., Illingworth, G. D., Franx, M., Chary, R., Meurer, G. R., Conselice, C. J., Ford, H., Giavalisco, M., & van Dokkum, P. 2009, ApJ, 705, 936

Byun, Y. I., Freeman, K. C., & Kylafis, N. D. 1994, ApJ, 432, 114

Calzetti, D., Kinney, A. L., & Storchi-Bergmann, T. 1994, ApJ, 429, 582

Carignan, C., & Purton, C. 1998, ApJ, 506, 125

Carswell, R. F., Whelan, J. A. J., Smith, M. G., Boksenberg, A., & Tytler, D. 1982, MNRAS, 198, 91

Cen, R., Miralda-Escudé, J., Ostriker, J. P., & Rauch, M. 1994, ApJ, 437, L9

Chen, H., Prochaska, J. X., & Gnedin, N. Y. 2007, ApJ, 667, L125

Christlein, D., & Zaritsky, D. 2008, ApJ, 680, 1053

Christlein, D., Zaritsky, D., & Bland-Hawthorn, J. 2010, MNRAS, 641

Corbelli, E., Schneider, S. E., & Salpeter, E. E. 1989, AJ, 97, 390

Croft, R. A. C., Weinberg, D. H., Katz, N., & Hernquist, L. 1998, ApJ, 495, 44

Davé, R., & Tripp, T. M. 2001, ApJ, 553, 528

Dierckx, P. 1993, Curve and surface fitting with splines (Monographs on Numerical Analysis, Oxford: Clarendon, —c1993)

Donahue, M., Aldering, G., & Stocke, J. T. 1995, ApJ, 450, L45+

Dove, J. B., & Shull, J. M. 1994, ApJ, 423, 196

Efstathiou, G. 1992, MNRAS, 256, 43P

Fardal, M. A., Giroux, M. L., & Shull, J. M. 1998, AJ, 115, 2206

Faucher-Giguère, C., Lidz, A., Hernquist, L., & Zaldarriaga, M. 2008a, ApJ, 682, L9

—. 2008b, ApJ, 688, 85

Faucher-Giguère, C., Lidz, A., Zaldarriaga, M., & Hernquist, L. 2008c, ApJ, 673, 39

—. 2009, ApJ, 703, 1416

Felten, J. E., & Bergeron, J. 1969, Astrophys. Lett., 4, 155

Gallego, J., Zamorano, J., Aragon-Salamanca, A., & Rego, M. 1995, ApJ, 455, L1+

García-Ruiz, I., Sancisi, R., & Kuijken, K. 2002, A&A, 394, 769

Gnedin, N. Y., Kravtsov, A. V., & Chen, H. 2008, ApJ, 672, 765

Haardt, F., & Madau, P. 1996, ApJ, 461, 20

Herbert-Fort, S., Zaritsky, D., Christlein, D., & Kannappan, S. J. 2010, ApJ, 715, 902

Hernquist, L., & Springel, V. 2003, MNRAS, 341, 1253

Hill, G. J., et al. 2008, in Proc. SPIE, Vol. 7014, 231

Hopkins, A. M. 2004, ApJ, 615, 209

Hopkins, P. F., Richards, G. T., & Hernquist, L. 2007, ApJ, 654, 731

Huchtmeier, R. 1989, A General Catalog of HI Observations of Galaxies. The Reference Catalog., ed. Huchtmeier, W. K., Richter, O.-G.

Hui, L., & Gnedin, N. Y. 1997, MNRAS, 292, 27

Kelson, D. D. 2003, PASP, 115, 688

Kennicutt, Jr., R. C. 1989, ApJ, 344, 685

Kulkarni, V. P., & Fall, S. M. 1993, ApJ, 413, L63

Lee, J. C., Gil de Paz, A., Tremonti, C., Kennicutt, R. C., Salim, S., Bothwell, M., Calzetti, D., Dalcanton, J., Dale, D., Engelbracht, C., Funes, S. J. J. G., Johnson, B., Sakai, S., Skillman, E., van Zee, L., Walter, F., & Weisz, D. 2009, ApJ, 706, 599

Loeb, A., & Eisenstein, D. J. 1995, ApJ, 448, 17

Madau, P., Haardt, F., & Rees, M. J. 1999, ApJ, 514, 648

Madsen, G. J., Reynolds, R. J., Haffner, L. M., Tufte, S. L., & Maloney, P. R. 2001, ApJ, 560, L135

Maloney, P. 1993, ApJ, 414, 41

Massey, P., Strobel, K., Barnes, J. V., & Anderson, E. 1988, ApJ, 328, 315

Matthews, L. D., Gallagher, III, J. S., & van Driel, W. 1999, AJ, 118, 2751

McCall, M. L., Rybski, P. M., & Shields, G. A. 1985, ApJS, 57, 1

O'Donnell, J. E. 1994, ApJ, 422, 158

Oosterloo, T., Fraternali, F., & Sancisi, R. 2007, AJ, 134, 1019

Osterbrock, D. E., & Ferland, G. J. 2006, Astrophysics of gaseous nebulae and active galactic nuclei

Rauch, M., Haehnelt, M. G., & Steinmetz, M. 1997a, ApJ, 481, 601

Rauch, M., Miralda-Escude, J., Sargent, W. L. W., Barlow, T. A., Weinberg, D. H., Hernquist, L., Katz, N., Cen, R., & Ostriker, J. P. 1997b, ApJ, 489, 7

Schirber, M., & Bullock, J. S. 2003, ApJ, 584, 110

Schlegel, D. J., Finkbeiner, D. P., & Davis, M. 1998, ApJ, 500, 525

Shapley, A. E., Steidel, C. C., Pettini, M., Adelberger, K. L., & Erb, D. K. 2006, ApJ, 651, 688

Shull, J. M., Roberts, D., Giroux, M. L., Penton, S. V., & Fardal, M. A. 1999, AJ, 118, 1450

Siana, B., Teplitz, H. I., Ferguson, H. C., Brown, T. M., Giavalisco, M., Dickinson, M., Chary, R., de Mello, D. F., Conselice, C. J., Bridge, C. R., Gardner, J. P., Colbert, J. W., & Scarlata, C. 2010, ArXiv e-prints

Stocke, J. T., Case, J., Donahue, M., Shull, J. M., & Snow, T. P. 1991, ApJ, 374, 72

Sunyaev, R. A. 1969, Astrophys. Lett., 3, 33

Thilker, D. A., Bianchi, L., Meurer, G., Gil de Paz, A., Boissier, S., Madore, B. F., Boselli, A., Ferguson, A. M. N., Muñoz-Mateos, J. C., Madsen, G. J., Hameed, S., Overzier, R. A., Forster, K., Friedman, P. G., Martin, D. C., Morrissey, P., Neff, S. G., Schiminovich, D., Seibert, M., Small, T., Wyder, T. K., Donas, J., Heckman, T. M., Lee, Y., Milliard, B., Rich, R. M., Szalay, A. S., Welsh, B. Y., & Yi, S. K. 2007, ApJS, 173, 538

Tully, R. B., Rizzi, L., Dolphin, A. E., Karachentsev, I. D., Karachentseva, V. E., Makarov, D. I., Makarova, L., Sakai, S., & Shaya, E. J. 2006, AJ, 132, 729

Uson, J. M., & Matthews, L. D. 2003, AJ, 125, 2455

van Gorkom, J. 1993, in Astrophysics and Space Science Library, Vol. 188, The Environment and Evolution of Galaxies, ed. J. M. Shull & H. A. Thronson, 345–+

Vogel, S. N., Weymann, R., Rauch, M., & Hamilton, T. 1995, ApJ, 441, 162

Walsh, W., Staveley-Smith, L., & Oosterloo, T. 1997, AJ, 113, 1591

Werk, J. K., Putman, M. E., Meurer, G. R., Ryan-Weber, E. V., Kehrig, C., Thilker, D. A., Bland-Hawthorn, J., Drinkwater, M. J., Kennicutt, R. C., Wong, O. I., Freeman, K. C., Oey, M. S., Dopita, M. A., Doyle, M. T., Ferguson, H. C., Hanish, D. J., Heckman, T. M., Kilborn, V. A., Kim, J. H., Knezek, P. M., Koribalski, B., Meyer, M., Smith, R. C., & Zwaan, M. A. 2010a, AJ, 139, 279

Werk, J. K., Putman, M. E., Meurer, G. R., Thilker, D. A., Allen, R. J., Bland-Hawthorn, J., Kravtsov, A., & Freeman, K. 2010b, ApJ, 715, 656

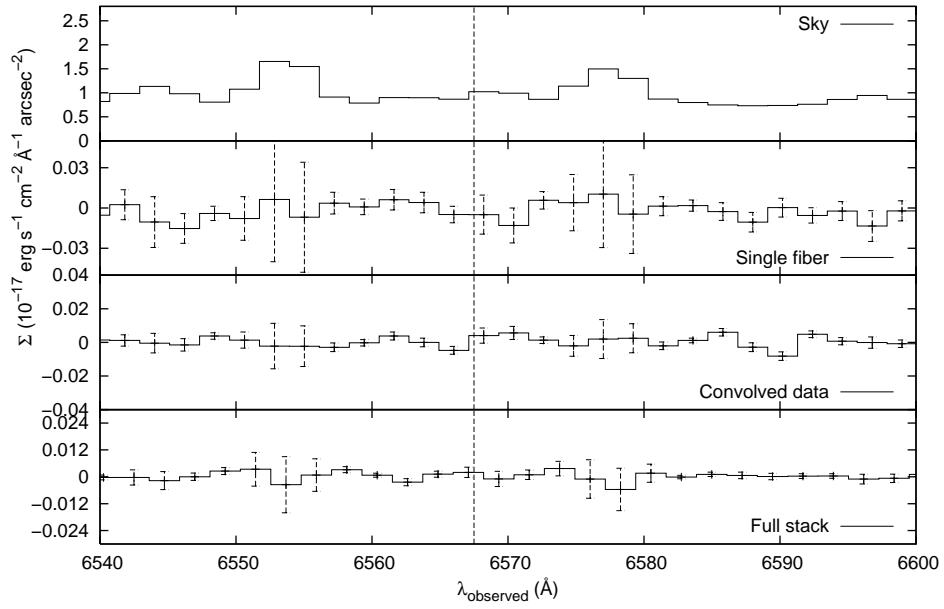Weymann, R. J., Vogel, S. N., Veilleux, S., & Epps, H. W. 2001, ApJ, 561, 559

Fig. 5.— Selected surface brightness spectra around Hα in UGC 1281. The format is the same as in Figure 4. In this case, 313 of the brightest expected fibers form the final stack.
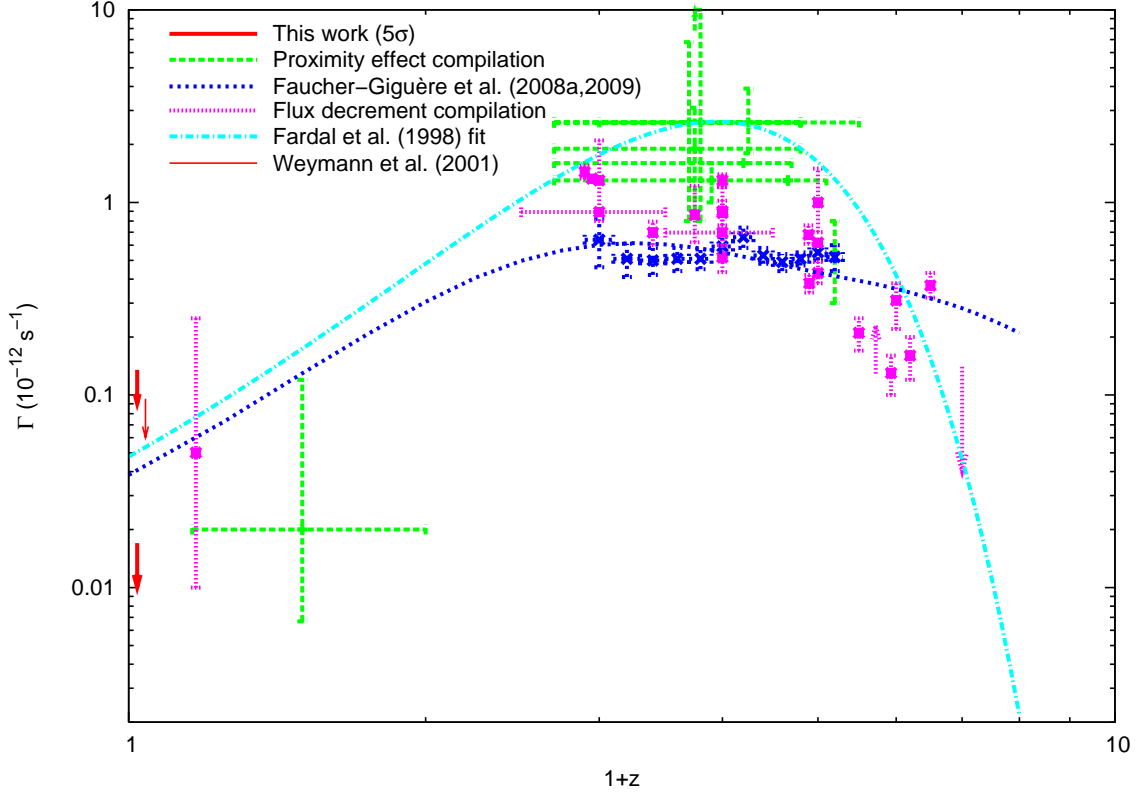
Fig. 6.— A compilation of photoionization rates across redshift. Most of the literature compilations come from Table 2 in Faucher-Giguère et al. (2008c) and Table 1 in Faucher-Giguère et al. (2008b). The flux decrement measurement at the lowest redshift is from Davé & Tripp (2001). The low redshift, Hα limit from Weymann et al. (2001) (2σ) has been the deepest z=0 limit before this work. Weymann et al. (2001). The UVB fitting function comes from Fardal et al. (1998) and the newer simulation from Faucher-Giguère et al. (2009). Our work's new limit is well outside the flux decrement normalized simulation and challenges one or more of the model assumptions. Some points have been slightly shifted in redshift for visual clarity.